Fe doping intensifies built-in electric field for tailoring the reconstruction of sulfides towards efficient oxygen evolution

Kun Wang, Chunmei Ni, Lei Jin, Xingyue Qian, Hui Xu*, Haiqun Chen*, and Guangyu He*

Key Laboratory of Advanced Catalytic Materials and Technology, Advanced Catalysis and Green Manufacturing Collaborative Innovation Center Institution, Changzhou University, 21 Gehu Lake Road, Changzhou, 213164, China

Corresponding authors: xuhui006@cczu.edu.cn (H. Xu); chenhq@cczu.edu.cn (H. Chen); hegy@cczu.edu.cn (G. He)

Electrochemical Measurements:

All the electrochemical tests were conducted on an electrochemical workstation (CHI 760E) with a standard three-electrode system in 1 M KOH. A carbon rod was used as the counter electrode, a Hg/HgO electrode (1 M KOH) was used as the reference electrode, and a glassy carbon electrode having a diameter of 5 mm was used as the working electrode.

All the potentials in this work were calibrated to a reversible hydrogen electrode (RHE) value according to the Equation (1):

$$E_{\mathrm{RHE}} = E_{\mathrm{Hg/HgO}} + 0.098 + 0.0591 \times \mathrm{pH} \tag{1}$$

Linear sweep voltammetry (LSV) was performed at a scan rate of 5 $mV \cdot s^{-1}$. Electrochemical impedance spectra (EIS) were recorded in a frequency range of 0.01 Hz-100 kHz with a 5 mV amplitude.

In addition, in-situ EIS testing was conducted under a potential range of 1.2-1.6 V with an interval of 0.1 V, while keeping other parameters constant. Double-layer capacitance (C_{dl}) was estimated based on the CV curves recorded in the non-faradaic region at various scan rates. Linear slope was extracted from the plot of capacitive current densities as a function of scan rates, where the was estimated as half of the linear slope. Chronopotentiometry was performed at the constant current density of 10 $mA \cdot cm^{-2}$ to evaluate the stability of the catalysts. The Mott-Schottky curves were tested in the above mentioned three-electrode instrument and acquired over an AC frequency of 1 kHz with the potential region of -1~0.5 V (vs. Ag/AgCl). The solution of 1 M KOH with 0.5 M NaCl was served as the simulated alkaline seawater electrolyte for OER test. All polarization curves in this work were not corrected with a 95 % iR compensation.

In addition, in order to study the oxidation-restructuring behavior of the catalyst of OER, the electrocatalyst was reconstructed by cyclic voltammetry (CV) experiments.

CV experiments were carried out in the applied voltage range of 1.1 to 1.7 V and 1 M KOH solution with a scan rate of 10 $\mathrm{mV \cdot s^{-1}}$.

In a three-electrode system with platinum mesh as the cathode, Ag/AgCl as the reference electrode, and platinum-carbon as the working electrode, the potential of zero charge (PZC) of the catalyst was measured through minimum differential capacitance measurements. To investigate the effect of BIEF on the surface OH^- of LDH, different concentrations of KOH (20, 40, 60, and 80 mM) were added to a 5 mM KCl electrolyte for testing. At a frequency of 1 Hz with a sinusoidal voltage perturbation of 5 mV and a potential increment of 5 mV, the electrochemical impedance-potential spectra were the testing method for PZC. The PZC value was determined from the minimum value of the specific capacitance (C_d), which was calculated from the imaginary part of the imaginary part (Z'') of the impedance spectra and angular frequency (ω, 1 Hz) according to Equation (2):

$$C_d = \left|\frac{1}{\omega Z''}\right| \tag{2}$$

Laviron equation according to Equation (3):

$$E_c = E_{\frac{1}{2}} - \left(\frac{RT}{\alpha nF}\right) \times ln\left(\frac{\alpha nF}{RTk_s}\right) - \left(\frac{RT}{\alpha nF}\right) \times ln(v) \tag{3}$$

where E_c is the reduction potential of metal redox, $E_{1/2}$ is the formal potential of metal redox, R is the universal gas constant, T is the temperature in Kelvin, n is the number of electrons transferred, α is the transfer coefficient, K_s is the rate constant of metal redox, and v is the scan rate in the CV measurements.

Randles-Sevcik equation to Equation (4):

$$I_p = (2.687 \times 10^5) n^{\frac{3}{2}} AC(vD)^{\frac{1}{2}} \tag{4}$$

where I_p, n, A and C are peak current density of M-OH formation, number of electrons participated, area of the electrode and the concentration of ions, respectively.

Characterization:

The morphologies of as-prepared samples were observed by field-emission scanning electron microscopy (FESEM, Zeiss Supra 55). Further studies on the morphology and structure were operated by a high-resolution transmission electron microscopy (HRTEM, FEI Talos F200x). The crystalline phases of the samples were investigated by powder X-ray diffraction (XRD) with Bruker D8 Advance diffractometer (Cu Kα radiation, $\lambda = 0.15418$ nm). X-ray photoelectron spectroscopy (XPS) was carried out on a Thermo Scientific K-Alpha. The Al Kα was used as an X-ray source ($hv = 1486.6$ eV). The concentrations of transition metals and sulfur in the electrolyte after stability testing were measured using the inductively coupled plasma optical emission spectrometer (ICP-OES, PerkinElmer). In Situ Raman Measurement: In situ Raman spectra were recorded on XpoloRA PLUS Raman spectrometer with 532 nm wavenumber of the excitation light source. In situ electrochemistry-Raman coupled experiments were conducted in a single-compartment, three-electrode, custom-made quartz cell controlled by an electrochemical workstation at room temperature. The loaded GCE, a graphite rod, and SCE were used as the working, counter, and reference electrodes, respectively. A stability potential in the range of 1.2-1.7 V with an interval of 0.1 V was applied to the catalyst electrode for 5 min before carrying out all in situ Raman spectra. Ultraviolet photoelectron spectroscopy (UPS) measurements were conducted using a Thermo Fisher Esca Lab 250Xi with a He (I) photo line of 21.22 eV. Ultraviolet-visible (UV-vis) spectroscopy measurements were performed using a Perkin Elmer Lambda 1050 on diffuse reflectance mode.

The work function was measured by ultraviolet photoelectron spectroscopy (UPS). A He discharge lamp with the He (I) photo line (21.22 eV) was applied, and the high-binding energy secondary electron cutoff (E_{cutoff}) and the energy gap (ΔE) between the valence band maximum (VBM) and the fermi level were extracted from the UPS spectra. The work function was calculated as Equation (5):

$$\Phi = 21.22eV - E_{cutoff} \tag{5}$$

The VBM position was calculated as Equation (6):

$$E_{VBM} = 21.22eV - \left(E_{cutoff} - \Delta E\right) \tag{6}$$

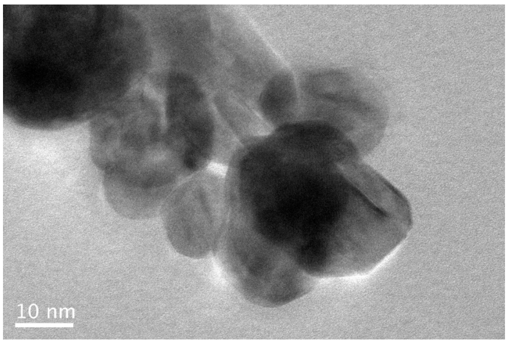

Fig. S1. TEM image of the Cr_2O_3.

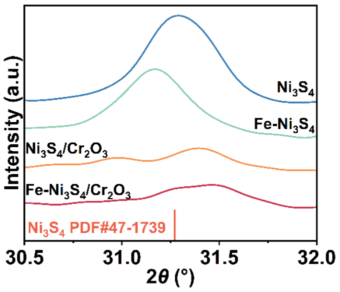

Fig. S2. Magnified XRD patterns of Ni_3S_4, Ni_3S_4/Cr_2O_3, Fe-Ni_3S_4, and Fe-Ni_3S_4/Cr_2O_3.

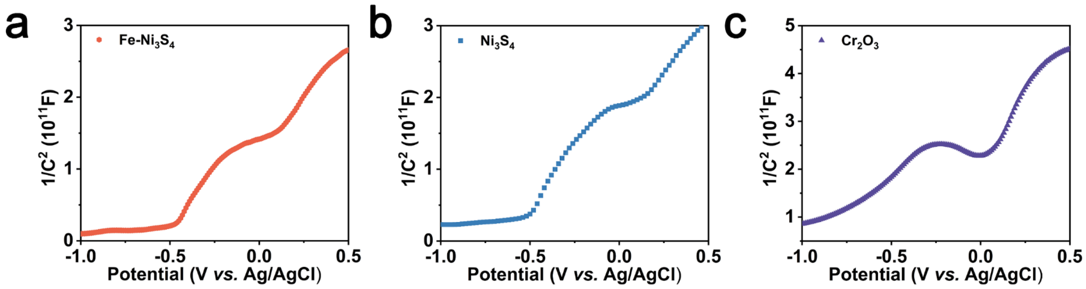

Fig. S3. Mott-Schottky plots of (a) Fe-Ni_3S_4, (b) Ni_3S_4 and (c) Cr_2O_3 electrocatalysts at the frequency of 1 kHz.

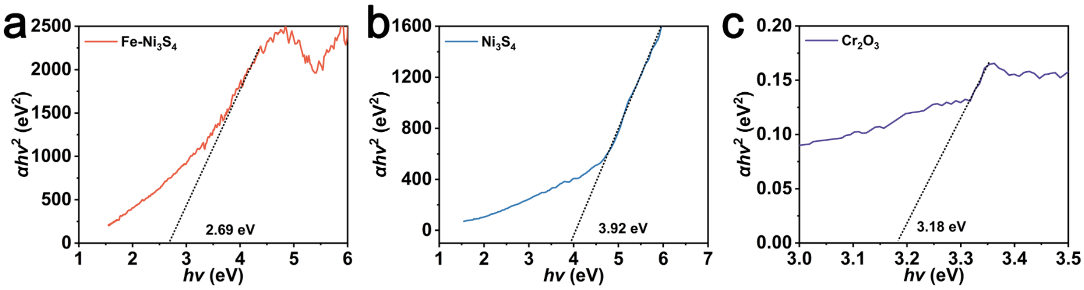

Fig. S4. Tauc plots of (a) Fe-Ni_3S_4, (b) Ni_3S_4, and (c) Cr_2O_3.

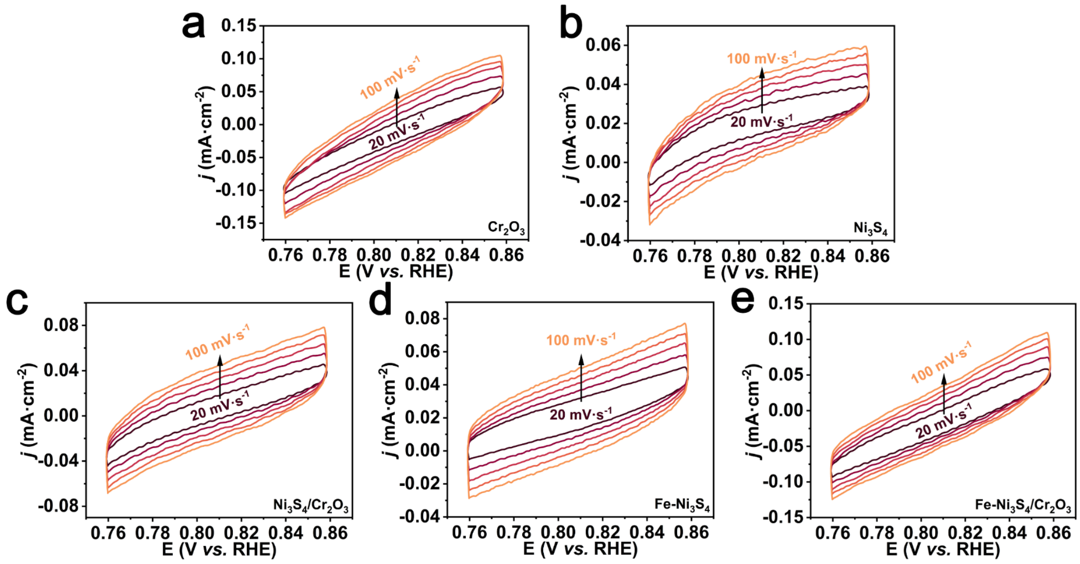

Fig. S5. Cyclic voltammograms in a non-Faradaic potential range at various scan rates from 20 to 100 mV·s^{-1} under the 1 M KOH electrolyte. (a) Cr_2O_3, (b) Ni_3S_4, (c) Ni_3S_4/Cr_2O_3, (d) Fe-Ni_3S_4, and (e) Fe-Ni_3S_4/Cr_2O_3.

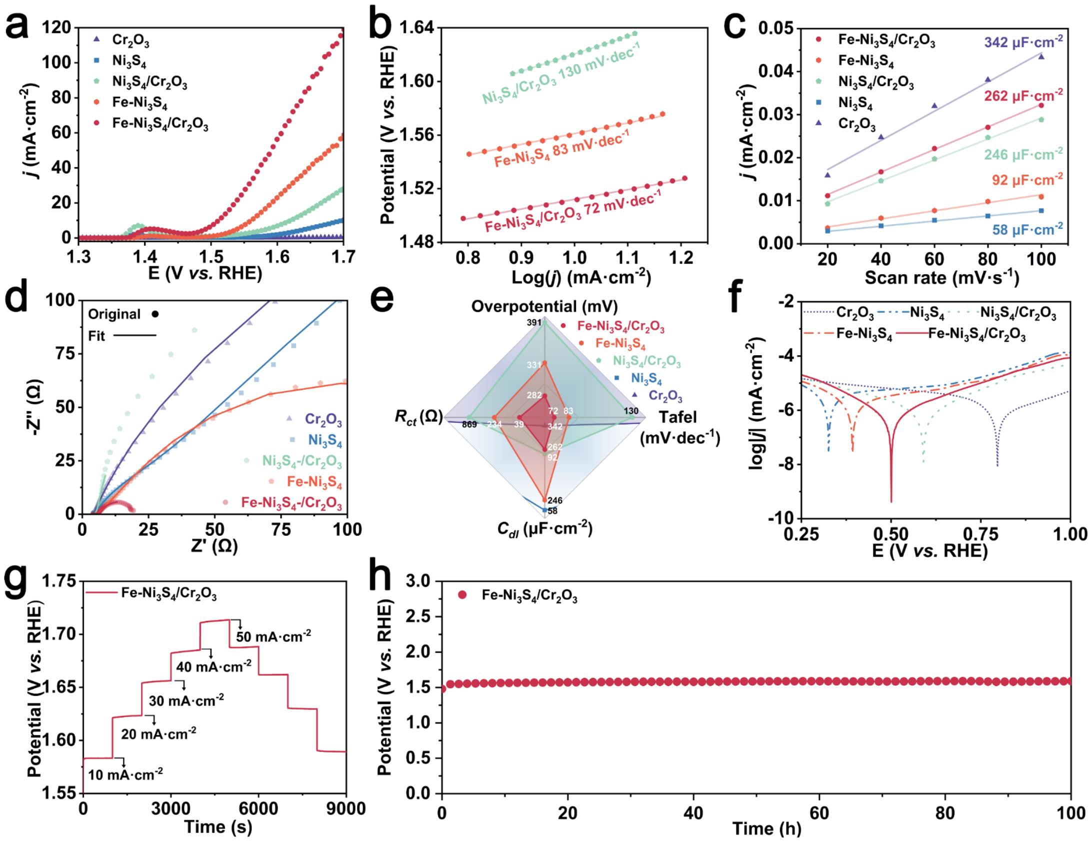

Fig. S6 OER activity in simulated seawater solution. (a) LSV polarization curves, (b) Tafel plots, (c) C_{dl} values, and (d) Nyquist plots at 1.5 V versus RHE of Cr_2O_3, Ni_3S_4, Ni_3S_4/Cr_2O_3, Fe-Ni_3S_4, and Fe-Ni_3S_4/Cr_2O_3. (e) Radar chart for comparison of comprehensive catalytic performance. (f) Corrosion polarization curves of Cr_2O_3, Ni_3S_4, Ni_3S_4/Cr_2O_3, Fe-Ni_3S_4, and Fe-Ni_3S_4/Cr_2O_3. (g) CP curve of Fe-Ni_3S_4/Cr_2O_3 at different current densities. (h) CP curve of Fe-Ni_3S_4/Cr_2O_3 at 10 mA·cm^{-2}.

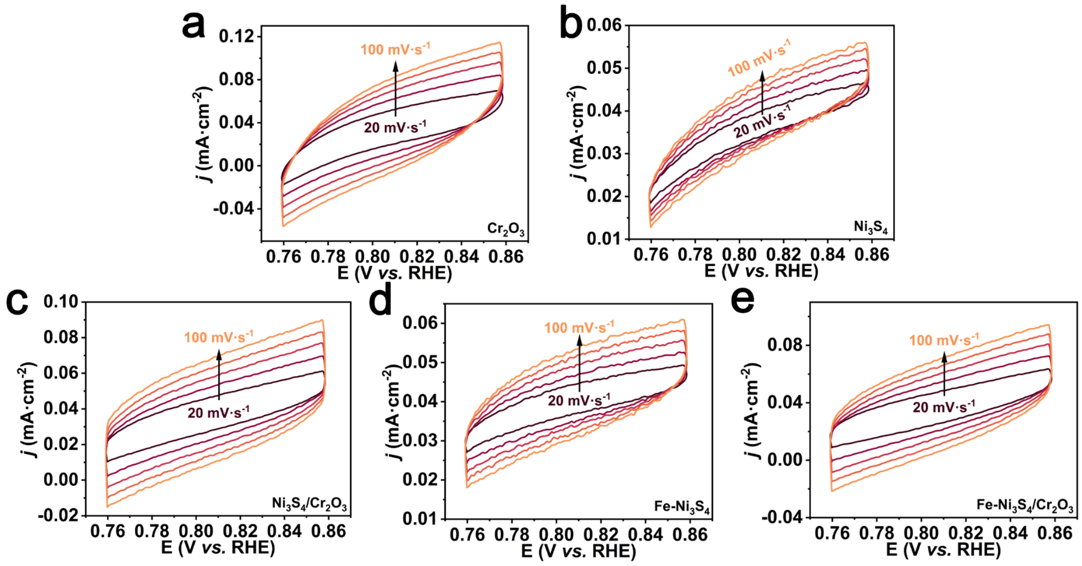

Fig. S7. Cyclic voltammograms in a non-Faradaic potential range at various scan rates from 20 to 100 mV·s^{-1} under the simulated seawater electrolyte. (a) Cr_2O_3, (b) Ni_3S_4, (c) Ni_3S_4/Cr_2O_3, (d) Fe-Ni_3S_4, and (e) Fe-Ni_3S_4/Cr_2O_3.

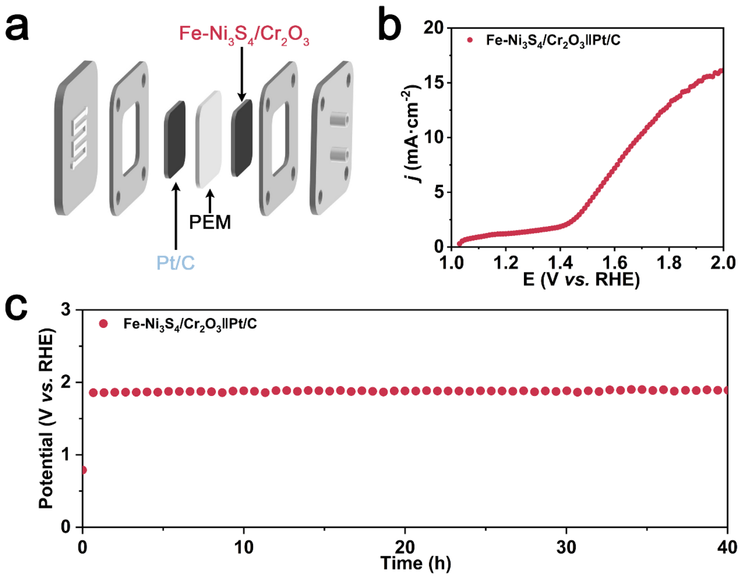

Fig. S8. (a) Schematic assembly of the overall water splitting in a commercial-scale AE. (b) Activity and (c) durability test for the commercial AE at a constant current density of 10 mA·cm^{-2}.

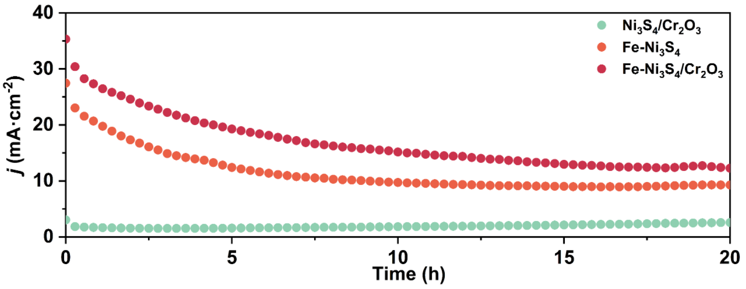

Fig. S9. Chronoamperometry test at 1.6 V of Ni_3S_4/Cr_2O_3, $Fe-Ni_3S_4$, and $Fe-Ni_3S_4/Cr_2O_3$.

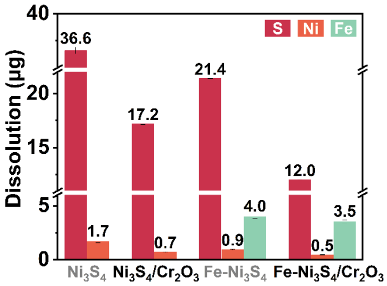

Fig. S10. Fe, Ni, S concentration in the electrolyte after 20 h chronoamperometry of Ni_3S_4, Ni_3S_4/Cr_2O_3, Fe-Ni_3S_4, and Fe-Ni_3S_4/Cr_2O_3.

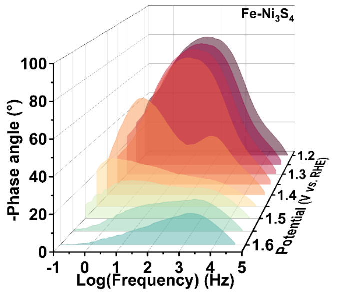

Fig. S11. Bode phase plots of the in-situ EIS on Fe-Ni_3S_4.

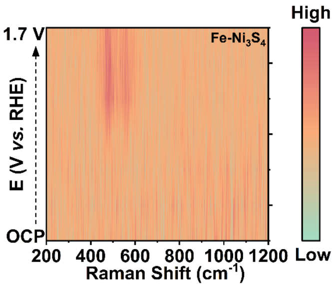

Fig. S12. Operando Raman spectra of Fe-Ni_3S_4.

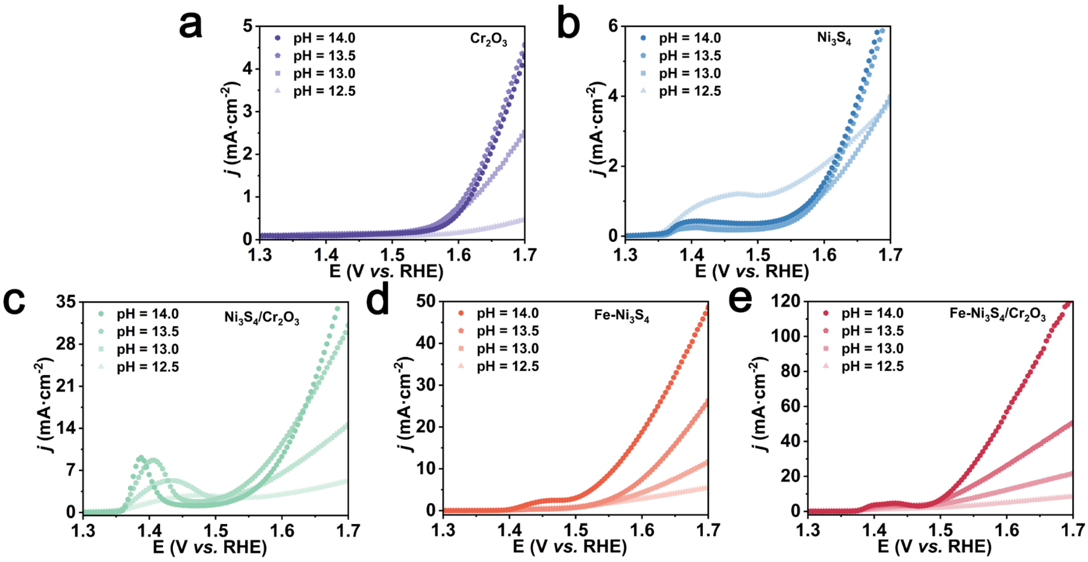

Fig. S13. LSV tests at different pH for (a) Cr_2O_3, (b) Ni_3S_4, (c) Ni_3S_4/Cr_2O_3, (d) Fe-Ni_3S_4, and (e) Fe-Ni_3S_4/Cr_2O_3.

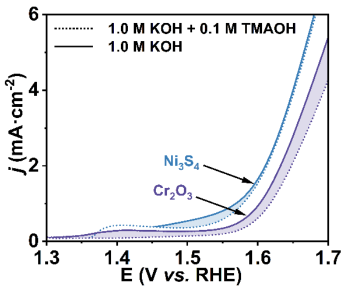

Fig. S14. Polarization curves for Cr_2O_3 and Ni_3S_4 in 1 M KOH with and without TMAOH.

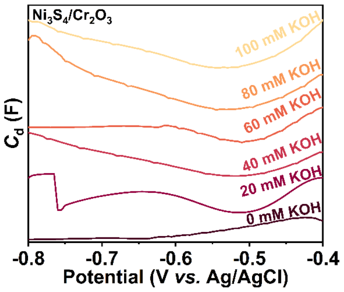

Fig. S15. Under different concentrations of KOH solutions, the differential capacitance (C_d) curves of Ni_3S_4/Cr_2O_3.

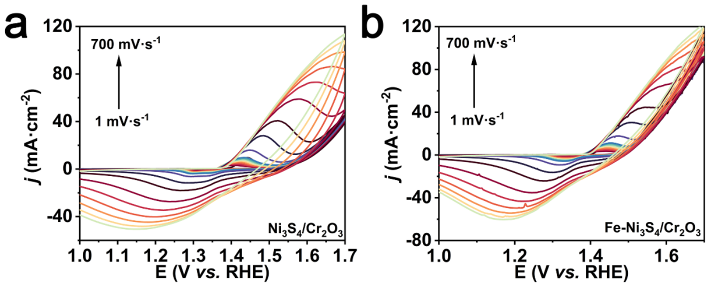

Fig. S16. CV tests at different scan rates in a 1 M KOH electrolyte. (a) Ni_3S_4/Cr_2O_3, (b) Fe-Ni_3S_4/Cr_2O_3.

Table S1 Performance comparison of Fe-Ni_3S_4/Cr_2O_3 with recently reported non-noble metal materials for electrocatalytic OER in 1 M KOH.

Catalysts	η (@10 mA·cm^{-2})	Tafel	Reference
Fe-Ni_3S_4/Cr_2O_3	282 mV	72 mV·dec^{-1}	This Work
$CuCo_2S_4$	310 mV	86 mV·dec^{-1}	ACS Catal., 2017, 7(9): 5871-5879.
Cr_2O_3/CrO_3/CrN@NCs	290 mV	84 mV·dec^{-1}	ACS Appl. Mater. Inter., 2024, 16(22): 28664-28672.
$NiCo_2S_4$@NiFe LDH	287 mV	87 mV·dec^{-1}	Appl. Catal., B, 2021, 286: 119869.
Co_9S_8/Ni_3S_4	334	119 mV·dec^{-1}	J. Alloys Compd., 2025, 1010: 177416.
Ni/NiO-C	370	114 mV·dec^{-1}	Inorg. Chem., 2024, 63(38): 17846-17855.